Free Radical Biology and Medicine 138 (2019) 10–22

Contents lists available at ScienceDirect

Free Radical Biology and Medicine

journal homepage: www.elsevier.com/locate/freeradbiomed

Original article

Effect of the additional cysteine 503 of vancomycin-resistant *Enterococcus faecalis* (V583) alkylhydroperoxide reductase subunit F (AhpF) and the mechanism of AhpF and subunit C assembling

Yew Kwang Toh[a], Joon Shin[b], Asha Manikkoth Balakrishna[b], Neelagandan Kamariah[b], Ardina Grüber[b], Frank Eisenhaber[a,c], Birgit Eisenhaber[a], Gerhard Grüber[a,b,*]

[a] Bioinformatics Institute, Agency for Science, Technology and Research (A*STAR), 30 Biopolis Street, #07-01 Matrix, Singapore, 138671, Republic of Singapore
[b] Nanyang Technological University, School of Biological Sciences, 60 Nanyang Drive, Singapore, 637551, Republic of Singapore
[c] School of Computer Science Engineering, Nanyang Technological University (NTU), 50 Nanyang Drive, Singapore, 637553, Republic of Singapore

ARTICLE INFO

Keywords:
Reactive oxygen species
Oxidative stress
Peroxiredoxins
Alkylhydroperoxide reductase
Enterococcus faecalis
Thioredoxin-like domain

ABSTRACT

The vancomycin-resistant *Enterococcus faecalis* alkyl hydroperoxide reductase complex (AhpR) with its subunits AhpC (*Ef*AhpC) and AhpF (*Ef*AhpF) is of paramount importance to restore redox homeostasis. Therefore, knowledge about this defense system is essential to understand its antibiotic-resistance and survival in hosts. Recently, we described the crystallographic structures of *Ef*AhpC, the two-fold thioredoxin-like domain of *Ef*AhpF, the novel phenomenon of swapping of the catalytic domains of *Ef*AhpF as well as the unique linker length, connecting the catalytically active N-and C-terminal domains of *Ef*AhpF. Here, using mutagenesis and enzymatic studies, we reveal the effect of an additional third cysteine (C503) in *Ef*AhpF, which might optimize the functional adaptation of the *E. faecalis* enzyme under various physiological conditions. The crystal structure and solution NMR data of the engineered C503A mutant of the thioredoxin-like domain of *Ef*AhpF were used to describe alterations in the environment of the additional cysteine residue during modulation of the redox-state. To glean insight into the epitope and mechanism of *Ef*AhpF and -AhpC interaction as well as the electron transfer from the thioredoxin-like domain of *Ef*AhpF to AhpC, NMR-titration experiments were performed, showing a coordinated disappearance of peaks in the thioredoxin-like domain of *Ef*AhpF in the presence of full length *Ef*AhpC, and indicating a stable *Ef*AhpF-AhpC-complex. Combined with docking studies, the interacting residues of *Ef*AhpF were identified and a mechanism of electron transfer of the *Ef*AhpF donor to the electron acceptor *Ef*AhpC is described.

1. Introduction

Enterococcus faecalis is a ubiquitous and opportunistic gram-positive microorganism responsible for 90% of nosocomial infections [1]. Compounding the pathogenicity of *E. faecalis* is its rapid development of resistance towards antimicrobial agents, the most common being the Vancomycin-Resistant Enterococcus (VRE) [2,3]. *E. faecalis* has evolved numerous virulence factors that ensure its survivability under harsh conditions of including reactive oxygen species (ROS) such as hydrogen peroxide (H_2O_2) inside macrophages [2,3]. The ability of *E. faecalis* to survive the intolerant ROS condition of the macrophage implies the presence of robust antioxidant systems [4] to which the Alkyl hydroperoxide reductase complex (AhpR) does belong too, which may serve as therapeutic targets for the prevention of early stages of infections [5,6].

The *E. faecalis* AhpR system is driven by two proteins, a 2-Cys peroxiredoxin, AhpC (*Ef*AhpC) and a thiol-dependent peroxiredoxin reductase, AhpF (*Ef*AhpF) to catalyse the NADH-dependent reduction of hydrogen peroxide [4] (Fig. 1A). The catalytic centre of AhpC is composed of two active cysteine residues; peroxidatic (C_P) and resolving (C_R). The peroxidatic cysteine residue (C_P) of one subunit of AhpC first reacts with a molecule of hydrogen peroxide to form sulfenic acid. Then a resolving cysteine residue (C_R) of the adjacent unit of AhpC attacks the sulfenic acid form, producing water molecule and oxidized AhpC [4,7]. As demonstrated by EM-data and the crystallographic structure, *Ef*AhpC forms a decamer independent to the redox state [7] (Fig. 1A). This is unlike AhpCs of gram-negative bacteria like *Escherichia coli* (*Ec*AhpC) and *Staphylococcus aureus* (*St*AhpC), which form a stable

* Corresponding author. Nanyang Technological University, School of Biological Sciences, 60 Nanyang Drive, Singapore, 637551, Republic of Singapore.
E-mail address: ggrueber@ntu.edu.sg (G. Grüber).

https://doi.org/10.1016/j.freeradbiomed.2019.04.036
Received 5 November 2018; Received in revised form 17 April 2019; Accepted 26 April 2019
Available online 30 April 2019
0891-5849/

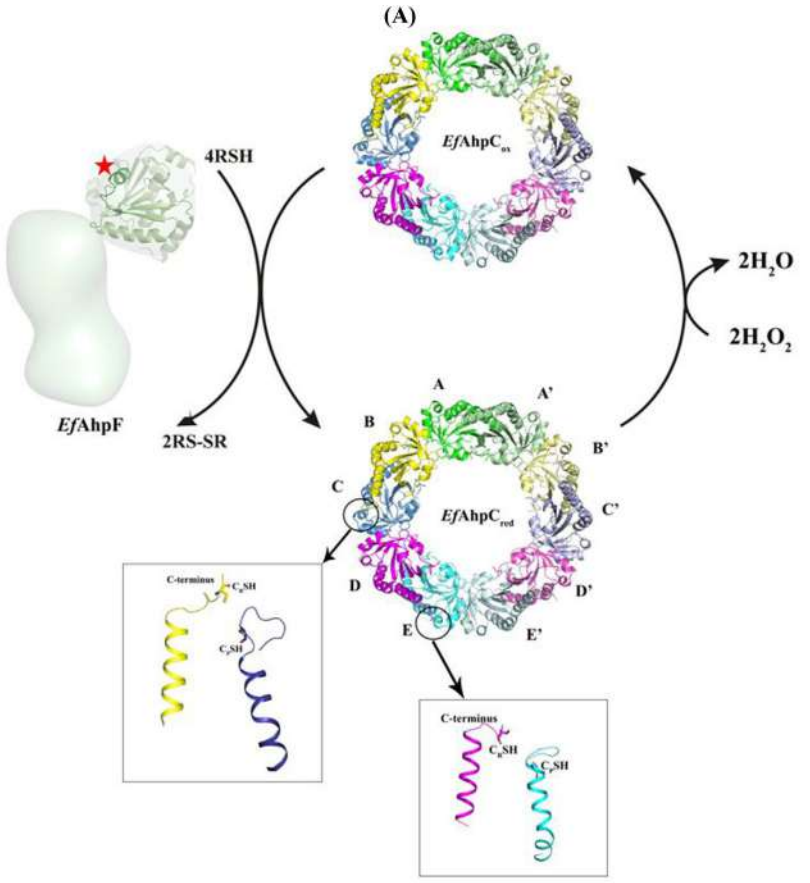

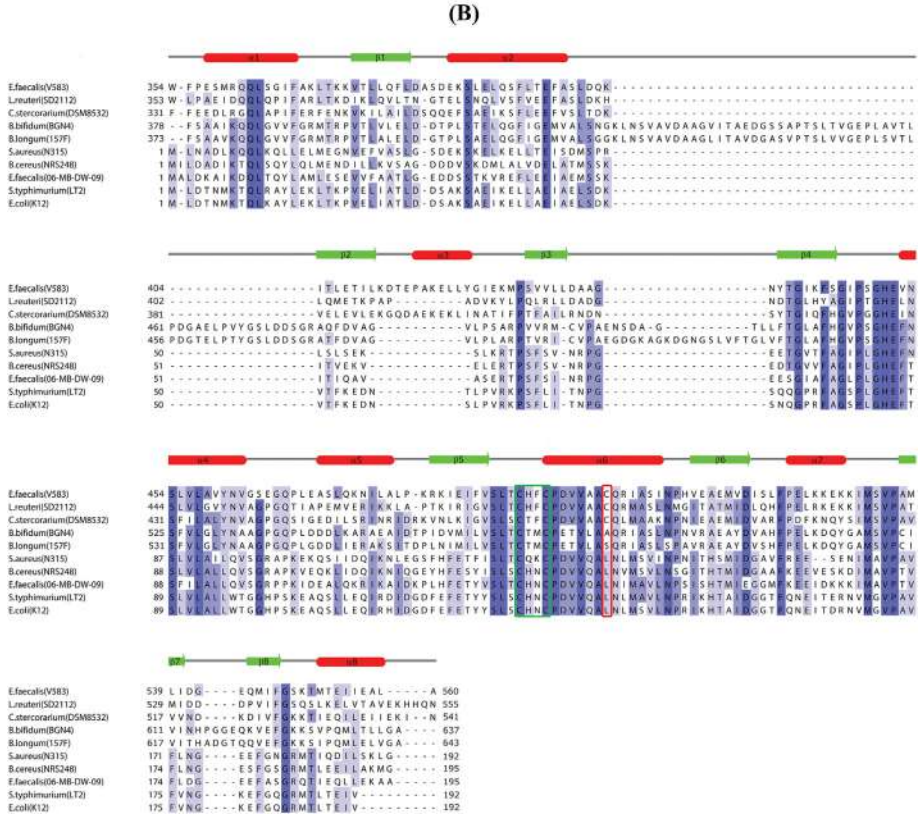

Fig. 1. The proposed catalytic cycle of the *Ef*AhpC-AhpF ensemble and multiple sequence alignment of the NTD_N/C domain of subunit AhpF. (*A*) *Ef*AhpC exists as a decameric ring in both oxidized and reduced states [7]. In the crystal structure of the reduced *Ef*AhpC$_{1\text{-}172}$ [7], the C_p loop exists in two different conformations as shown in the *inset boxes*. In the reduced state of *Ef*AhpC the peroxidative cysteine C_P in the fully folded (FF) conformation attacks H_2O_2 and reduces it to H_2O. In this process, C_P is converted into sulfenic acid (C_P-SOH form). The resolving cysteine, C_R, then attacks the C_P-SOH form to generate an inter-molecular disulphide bond. Subsequently, this disulphide bonded form of C_P undergoes a conformational change to a locally unfolded form (LU). This disulphide is then resolved by the interacting partner, AhpF. The recently determined low resolution solution structure of the dimeric *Ef*AhpF with the crystal structure of *Ef*AhpF$_{354\text{-}560}$ [13] inside. The unique loop in *Ef*AhpF$_{354\text{-}560}$ with the short helix $_{409}$ILKDTEPAKELLYGIEKM$_{426}$ is marked with an asterisk. (*B*) Multiple sequence alignment of the NTD_N/C domain of subunit AhpF from ten different species was performed using T-coffee algorithm [37] embedded within Jalview program [38]. The secondary structure elements of *Ef*AhpF$_{354\text{-}560}$ are shown above the sequence. Conserved residues are highlighted in *blue*. The CXXC conserved motif is outlined in *green* box. *Ef*AhpF C503 and its equivalent residues from other species are outlined in *red* box. (For interpretation of the references to colour in this figure legend, the reader is referred to the Web version of this article.)

decamer in the reduced form and lower weight oligomers in the oxidized state [8–10]. In comparison, besides the two typical catalytic cysteine residues C_P and C_R, *Ef*AhpC has two additional cysteines, with C13 and C66 at the N-terminus, which are important for stabilization of the decameric ring and enzyme activity [7].

Oxidized AhpC is regenerated via the reducing action of AhpF [11]. The latter is a homodimeric protein which is composed of two domains with a flexible linker in-between [12,13]. The electron donor NADH first docks at its binding site located at the pyridine nucleotide-disulfide oxidoreductase domain (CTD:Pyr_redox_2). This sets off cascading steps of electron transfer from the NADH molecule via FAD (flavin adenine dinucleotide), a prosthetic group to the first CXXC-motif located at the same domain. The second CXXC-motif residing at the two-fold thioredoxin-like domain (NTD_N/C) will then come close to the first reduced CXXC-motif and pick up the electron. This allows the reduced second CXXC-motif to regenerate the reducing potential of oxidized AhpCs [11,13,14].

We had first described the unique phenomenon of AhpF protein in *E. faecalis* (V583) bacteria (*Ef*AhpF), highlighting the distinct structural features such as domain swapping, and the unusual long flexible linker connecting the catalytic NTD_N/C and CTD:Pyr_redox_2 domains [13]. Our recent crystallographic structure of the *Ef*AhpF NTD_N/C part unravelled a unique loop-helix stretch ($_{409}$ILKDTEPAKELLYGIEKM$_{426}$) not present in homologue domains of other prokaryotic AhpFs. Deletion of the $_{415}$PAKELLY$_{421}$-helix affected protein stability or attenuates peroxidase activity [13].

Besides the significant differences of *Ef*AhpF compared to its counterpart in other AhpFs described above, *Ef*AhpF harbours one additional cysteine, C503, in the NTD_N/C domain. In analogy to the two additional cysteines (C13, C66) of *Ef*AhpC, relevant for stabilization of the decameric ring and enzyme activity [7], we sought to investigate the significance of C503 of *Ef*AhpF using a complementary approach of mutagenesis, enzyme assays, crystallography, and NMR solution spectroscopy. In addition, the complex formation of *Ef*AhpF-AhpC is closely studied here using NMR analysis. Coupled with our previous published results, these data will lead to a better understanding of the *E. faecalis* (V583) AhpR system in *E. faecalis* (V583) which can then be exploited as a therapeutic target.

2. Materials and Methods

2.1. Cloning of EfAhpF, AhpC and their mutants

Wild type (WT) *Ef*AhpF and *Ef*AhpF$_{354\text{-}560}$ were cloned into the pET9-d1-His6 vector [15] as described in the paper [13]. Cloning of *Ef*AhpC and its single mutants C13N and C66V as well as double mutant C13N/C66V was performed as described recently by Pan et al. [7]. Full-length *Ef*AhpF C503A and *Ef*AhpF$_{354\text{-}560}$ C503A were cloned with forward primer (5' – GTCGTGGCGGCTGCCCAACGTATT – 3′) (underlined indicates single amino acid substitution) and reverse primer (5' - ATC GGGACAGAAATGACATGTTAGTGAAACAAAGATTTC – 3'), using respective wild-type *Ef*AhpF vector as template by non-overlapping site-directed mutagenesis. The PCR products were *Dpn*I-digested before purified and transformed into *E. coli* DH5α cells.

2.2. Purification of WT and mutant proteins of E. faecalis

WT *E. faecalis* AhpR subunits AhpC and F as well as their mutants were transformed into *E. coli* BL21 (DE3) cells (Stratagene, USA) and induced with 1 mM isopropyl β-D-1-thiogalactopyranoside (IPTG) at 20 °C (*Ef*AhpF) or 37 °C (*Ef*AhpC) for protein production. Cells were lysed on ice by sonication for 3 × 1 min in buffer A (50 mM Tris/HCl, pH 7.5, 200 mM NaCl, 0.8 mM DTT and 2 mM Pefabloc^{SC} (BIOMOL)). The cell lysate was centrifuged at 10 000 × *g* for 35 min before the supernatant was filtered (0.45 µm; Millipore) and incubated with Ni-NTA Agarose (Qiagen) for 1 h at 4 °C. His$_6$-tagged protein was then eluted with an imidazole gradient (20 mM–500 mM) in Buffer A. For *Ef*AhpC, pooled fractions containing the protein of interest were applied onto a gel filtration column (Superdex™ 200 HR 10/300 column, GE Healthcare) in buffer B (50 mM Tris/HCl, pH 7.5 and 200 mM NaCl). In the case of *Ef*AhpF, fractions containing the recombinant protein were pooled and applied onto an anion chromatography column ResourceQ (6 ml). Fractions containing recombinant protein were pooled and applied onto a gel filtration column (Superdex™ 200 HR 10/300 column, GE Healthcare) in buffer B, and the purified recombinant protein was pooled and concentrated. All other *Ef*AhpF mutans were purified according to the WT *Ef*AhpF purification protocol [13].

2.3. Crystallization of EfAhpF$_{354\text{-}560}$ C503A

Recombinant *Ef*AhpF$_{354\text{-}560}$ (NTD_N/C) C503A mutant was concentrated to 5 mg/ml in a buffer composed of 50 mM Tris/HCl, pH 7.5 and 200 mM NaCl. Hexagonal-shaped crystals were grown in precipitant solution of 0.1 M Bis-Tris (pH 6.5), 1.5 M ammonium sulfate and 0.1 M sodium chloride by hanging-drop vapor-diffusion method. The final *Ef*AhpF$_{354\text{-}560}$ C503A crystals were flash-frozen in liquid nitrogen at 100 K in crystallization buffer containing 0.1 M Bis-Tris (pH 6.5), 2.0 M ammonium sulfate, 0.1 M sodium chloride and 2.0 M Proline.

2.4. Data collection and structure determination of EfAhpF$_{354\text{-}560}$ C503A

X-ray diffraction data for the *Ef*AhpF$_{354\text{-}560}$ C503A were collected at 100 K at beamline 13B1 of the National Synchrotron Radiation Research Centre (NSRRC, Hsinchu, Taiwan) using the ADSC Quantum 315 CCD detector. Data were collected as a series of 0.5° oscillation images covering a crystal rotation range of 100° on cryo-cooled crystals. A complete 2.5 Å data set was collected and the diffraction data were indexed, integrated and scaled using HKL2000 suite [16]. The results of data processing and data statistics are summarized in Table 1. The crystallographic structure was solved by molecular replacement method using WT *Ef*AhpF$_{354\text{-}560}$ structure (PBD ID: 5H29) [13] as model in PHASER [17]. The starting model was improved by iterative cycles of model building manually using Coot [18] and refinement by REFMAC5 [19] of CCP4 suite. Refinement was done until convergence and the geometry of the final model was validated with MolProbity [20]. This analysis indicated that the overall geometry of the final model ranked in the 100th percentile (MolProbity score of 1.23). The clash score for all atoms was 1.22 corresponding to a 100th percentile ranking of structures of comparable resolution. The data were cut off at 2.5 Å based on the $CC_{1/2}$ statistics [20] (correlation coefficient between two random halves of the data set where $CC_{1/2}$ > 10%) to determine the high-resolution cut-off for our data. Phenix [21] was used to compute $CC_{1/2}$ (97.5% for the highest resolution shell and 99.9% for the entire data set), supporting our high-resolution cut-off determination. The figures were drawn using PyMOL [22] and structural comparison analysis was carried out using SUPERPOSE [23] from CCP4 suite [24,25]. The coordinates and structure factors of *Ef*AhpF$_{354\text{-}560}$ C503A at 2.5 Å have been deposited in the Protein Data Bank with accession code [6IL7].

2.5. NADH-dependent peroxidase assay

NADH-dependent peroxidase assay was monitored at 340 nm following the decrease in NADH absorbance using a stopped flow spectrophotometer Applied Photophysics SX20. The assay was carried out at 25 °C containing a 100 mM phosphate buffer at pH 7.0, 200 mM ammonium sulfate and 1 mM EDTA. One syringe arm contained a final concentration of 200 µM of NADH, 100 µM of H_2O_2, increasing concentration of AhpC [1–80 µM], and the other arm contained a final concentration of 100 nM WT *Ef*AhpF or *Ef*AhpF C503A mutant. The assay was done in triplicates. Michaelis-Menten plots were created

Table 1
Data collection and refinement statistics.

Wavelength (Å)	1.00
Space group	$P4_132$
Unit cell parameters (Å)	$a = b = c = 134.101$ $\alpha = \beta = \gamma = 90^{\circ}$
Resolution range (Å)	30–2.5
Solvent content (%)	72.06
Total number of reflections	166,667
Number of unique reflections	14,035
I/σ(I)[a]	22.4 (7.3)
Completeness (%)	99.7 (99.7)
R_{merge}[b] (%)	6.9 (25.2)
Redundancy	11.2 (11.7)
Refinement Statistics	
R factor[c] (%)	21.47
R free[d] (%)	26.72
Number of amino acid residues	207
Ramachandran statistics	
Favoured (%)	98.1
Generously (%)	1.9
Disallowed (%)	0.0
R.M.S. Deviations	
Bond lengths (Å)	0.006
Bond angles (°)	1.088
Mean atomic B values	
Overall	61.02
Wilson B Factor	48.63
CC1/2	99.9 (97.5)
CC*	100 (99.4)
Clash score	1.22
Molprobity score:	1.23

[a] Values in parentheses refer to the corresponding values of the highest resolution shell (2.59–2.5 Å).

[b] $R_{merge} = \Sigma\Sigma_i|I_h - I_{hi}|/\Sigma\Sigma_i I_h$, where I_h is the mean intensity for reflection h.

[c] R-factor = $\Sigma||F_O| - |F_C||/\Sigma|F_O|$, where F_O and F_C are measured and calculated structure factors, respectively.

[d] R-free = $\Sigma||F_O| - |F_C|/\Sigma|F_O|$, calculated from 5% of the reflections selected randomly and omitted during refinement.

using program Origin Pro 9.0 (OriginLab Corporation).

2.6. Ferrous oxidation xylenol orange (FOX) assay

Hydrogen peroxide reduction catalysed by *Ef*AhpC in the presence of *Ef*AhpF was measured in PeroxiDetect™ kit by Sigma-Aldrich®. The kit is based on the principle of ferrous oxidation xylenol orange assay. 100 µl of reaction mixture containing 50 mM HEPES buffer pH 7.0, 100 µM H_2O_2, 250 µM NADH, 15 µM WT *Ef*AhpC or *Ef*AhpC mutants and 0.4 µM WT *Ef*AhpF or *Ef*AhpF C503A were prepared from which 10 µl of aliquots were removed at specific time intervals and added to 190 µl of FOX reagent before incubating for at least 30 min at room temperature. The absorbance of the sample was then measured at λ = 560 nm for detection of H_2O_2.

2.7. NMR analysis of $EfAhpF_{354\text{-}560}$

0.7 mM of $^{15}N/^{13}C$ double-labelled $EfAhpF_{314\text{-}560}$ was prepared in 50 mM sodium phosphate pH 6.8, 50 mM NaCl, 10% D_2O in the presence or absence of 2 mM TCEP (tris(2-carboxyethyl)phosphine) according to the purification method described above. NMR measurements were performed on 700 MHz Bruker Avance NMR spectrometer equipped with 5 mm triple-resonance ($^1H/^{15}N/^{13}C$) single axis gradient cryogenic probes at 298K.

To assign the backbone of $EfAhpF_{354\text{-}560}$, both uniform (traditional) and non-uniform sampling (NUS; [26]) techniques were employed to acquire the data. 2D-^1H-^{15}N TROSY-HSQC data were collected with conventional linear sampling technique, whereas all triple resonance experiments, including TROSY-HNCACB, 3D-TROSY-HN(CO)CACB, CBCA(CO)NH, HNCA and HN(CO)CA data were collected using NUS techniques of the indirect dimension as 20% sampling rates and reconstructed using compressed sensing (CS) scheme using MDDNMR software [27,28]. All NMR-spectra were processed using NMRpipe [29] and analyzed with SPARKY program [30]. Both techniques enabled the assignment of 90% of the backbone resonances (N, CA, HN).

Titration of 0.3 mM uniformly ^{15}N-labelled $EfAhpF_{354\text{-}560}$ or $EfAhpF\text{-}C503A_{354\text{-}560}$ with oxidized *Ef*AhpC was performed to achieve incremental molar equivalents of 0.05 and 0.1. ^1H-^{15}N TROSY-HSQC spectra were recorded with 2,048 complex data points in t_2 and 256 t_1 increments at molar ratios of 1 (*Ef*AhpF): 0 (*Ef*AhpC), 1:0.05 and 1:0.1, respectively. Spectral width of 2,270 and 11,160 Hz were employed in F1(^{15}N) and F2(^1H), respectively. The combined chemical shift perturbation, the peak intensity and line width informations were extracted to determine molecular interaction between two proteins.

2.8. High ambiguity driven DOCKing(HADDOCK) modeling of $EfAhpF_{354\text{-}560}$ and $EfAhpC_{1\text{-}167}$

Experimentally identified binding interfacial residues of $EfAhpF_{354\text{-}560}$, excluding the extra flexible loop from amino acids A314-Q353, were used to perform docking studies, and to model the complex of $EfAhpF_{354\text{-}560}$ and $EfAhpC_{1\text{-}167}$ using the HADDOCK webserver [31]. The experimentally determined crystal structures for the $EfAhpF_{354\text{-}560}$ and $EfAhpC_{1\text{-}167}$ dimer were used for docking simulation. Surface exposed residues experiencing intensity and linewidth changes during titration were used as restraints. Since HADDOCK requires a set of ambiguous interaction restraints, residues directly interacting at the interface need to be specified as “active” residues and neighbouring residues as “passive”. The experimentally obtained interacting residues were set as active. In the case of $EfAhpC_{1\text{-}167}$, a dimeric unit of coordinates from the crystal structure were submitted to the meta-PPISP for protein–protein interfacial residues prediction [32]. These predicted interfacial residues were set as “active” residues. These restraints were used as input for the HADDOCK webserver and default parameters were used for docking. The resulting structures were clustered by a cut-off value (7.5 Å). Finally, based on the HADDOCK score and total energy, the best model from the highest scoring cluster was selected for analysis. The model was visualized using the PyMOL software [22].

3. Results

3.1. Sequence analysis of E. faecalis AhpF's two-fold thioredoxin-like domain (NTD_N/C)

Inspection of the *Ef*AhpF protein sequence showed that its two-fold thioredoxin-like domain (NTD_N/C) contains an additional cysteine residue at position 503 in helix α6 (Fig. 1B). To investigate whether the occurrence of this additional cysteine residue is predominant in AhpFs of other species, a protein sequence alignment of AhpF NTD_N/C domains of ten different species was performed. It was shown that domain swapping is a unique feature of *Ef*AhpF where the NTD_N/C is located at the C-terminus and the pyridine nucleotide-disulfide oxidoreductase domain (CTD:Pyr_redox_2) is located at the N-terminus [13]. Therefore, AhpF NTD_N/C domains of five different species displaying the ‘*E. faecalis*-like’ AhpF domain localization (C-terminus) and AhpF NTD_N/C domains of another five different species showing ‘*E. coli*-like’ AhpF domain localization (N-terminus) were chosen for this sequence alignment. The alignment indicates that the additional cysteine at position 503 is conserved across several species belonging to the ‘*E. faecalis*-like’ subgroup, *E. faecalis* (V583), *L. reuteri* (SD2112) and *C. stercorarium* (DSM8532), but is not present in the *Bacillus* species and all sequences

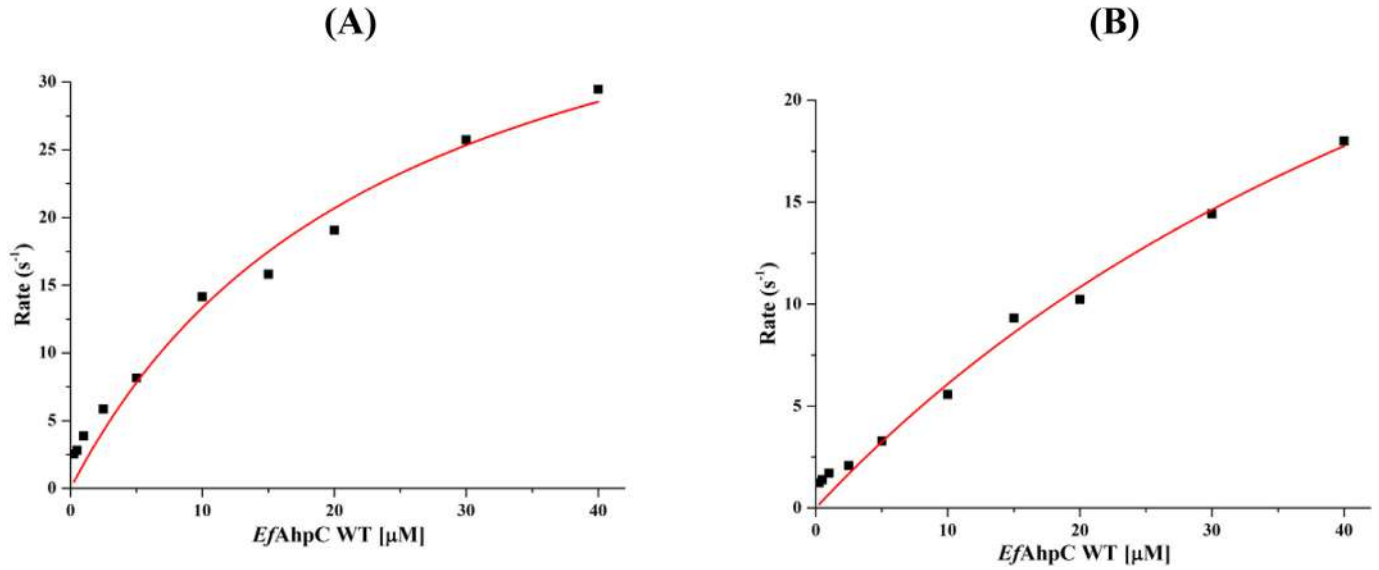

Fig. 2. Enzymatic characterization of WT *Ef*AhpF and its mutant. Michaelis-Menten plot of 0.5–40 μM of *Ef*AhpC WT with 50 nM of (*A*) *Ef*AhpF WT or (*B*) *Ef*AhpF C503A. Data shown are mean of triplicates.

of the '*E. coli*-like' subgroup (Fig. 1B, red box). Interestingly, both *B. bifidum* (BGN4) and *B. longum* (157F) NTD_N/C harbour two additional cysteine residues in position 496 and 609 according to *B. bifidum* (BGN4) numbering. To note, in all AhpF NTD_N/C domains of the species belonging to the '*E. coli*-like' subgroup the cysteine residue is replaced by a leucine residue.

3.2. Importance of the extra cysteine 503 in *Ef*AhpF

To investigate the importance of the extra cysteine C503, this residue was mutated to alanine (C503A) in the full-length *Ef*AhpF construct. Kinetic studies using NADH-based oxidation assay on stopped-flow spectrometer was performed (Fig. 2). WT *Ef*AhpF displays a k_{cat} of 46.1 ± 4 s^{-1} and a K_m (AhpC) of 24.5 ± 5 μM, giving it an enzymatic efficiency, k_{cat}/K_m (AhpC) of 1.9×10^6 M^{-1} s^{-1} (Fig. 2A). In contrast, the *Ef*AhpF C503A mutant has a similar k_{cat} of 49.2 ± 6 s^{-1} but an ~3-fold higher K_m (AhpC) of 70.9 ± 12 μM, which translates to a nearly 27-fold lower catalytic efficiency of *Ef*AhpF C503A where k_{cat}/K_m (AhpC) is 0.7×10^5 M^{-1} s^{-1} (Table 2) (Fig. 2B). The increased K_m (AhpC) of *Ef*AhpF C503A suggests that the mutation leads to a negative effect on its interaction with *Ef*AhpC.

To further confirm that the C503 mutation affects the reduction of *Ef*AhpC, a FOX assay was performed to measure the ability of *Ef*AhpF C503A together with *Ef*AhpC to reduce H_2O_2 (Fig. 3A). WT *Ef*AhpF reduced 5 μM of H_2O_2 in about 1 min, whereas *Ef*AhpF C503A reduced the same concentration of H_2O_2 in about 3 min. This correlates with the stopped-flow kinetic studies, showing that C503 is important for the catalytic activity of *Ef*AhpF.

Our recent studies revealed, that extra cysteine residues from *Ef*AhpC (C13 and C66) have an important role in the *Ef*AhpR system as mutation of these cysteine residues to its equivalent residues in *E. coli* AhpC (C13N and C66V) adversely affected the *Ef*AhpR system to reduce H_2O_2 [7]. Here, *Ef*AhpF C503A was analyzed by the FOX assay in the presence of the *Ef*AhpC mutants C13N (*Ef*AhpC C13N), *Ef*AhpC C66V, and the double mutant *Ef*AhpC C13N/C66, respectively (Fig. 3B). When compared to *Ef*AhpC-AhpF C503A, the mutant ensemble *Ef*AhpC C66V-AhpF C503A revealed a reduction in H_2O_2 decomposition which became even more prominent for mutant complexes *Ef*AhpC C13N-AhpF C503A followed by *Ef*AhpC C13N/C66-AhpF C503A, indicating an additive effect on the *Ef*AhpC cysteine mutants' ability to reduce H_2O_2.

Table 2
Kinetic constants for WT *Ef*AhpF and mutant *Ef*AhpF C503A.

*Ef*AhpF	k_{cat} (s^{-1})	K_m (AhpC) (μM)	k_{cat}/K_m (AhpC)(M^{-1}·s^{-1})
WT	46.1 ± 4	24.5 ± 5	1.9×10^6
C503A	49.2 ± 6	70.9 ± 12	0.7×10^5

3.3. Crystallographic structure of the *Ef*AhpF$_{354\text{-}560}$ C503A mutant

To investigate whether the substitution of C503 to alanine causes a structural change in *Ef*AhpF NTD_N/C, we crystallized *Ef*AhpF$_{354\text{-}560}$ C503A in the same crystallization solution as WT *Ef*AhpF$_{354\text{-}560}$ [13]. Crystals grew to the same cubic space group $P4_132$ and the determined atomic structure was refined to 2.5 Å resolution. The final R-factor and R-free (calculated with 5% of reflections that were not included in the refinement) were 21.47% and 26.72%, respectively (Table 1). There is one molecule of *Ef*AhpF$_{354\text{-}560}$ C503A in the asymmetric unit with a solvent content of 72.06%. The *Ef*AhpF$_{354\text{-}560}$ C503A monomer contained 207 amino acid residues with almost all main chain residues fitting well into the electron density. The *Ef*AhpF$_{354\text{-}560}$ C503A monomer also contained three molecules of SO_4 and 67 molecules of water (Table 1). The overall structure of *Ef*AhpF$_{354\text{-}560}$ C503A is shown in Fig. 4A. The side chain density for all the amino acids is very well resolved. The average B-factor was calculated to be 61.02 $Å^2$. Analysis of the stereo-chemical quality of the final model by PROCHECK has identified that 98.1% of all the residues are within the favoured regions of the Ramachandran plot, 1.9% are within the generously allowed regions. There were no residues in the disallowed region.

When *Ef*AhpF$_{354\text{-}560}$ C503A was overlaid with WT *Ef*AhpF$_{354\text{-}560}$, it aligned well with an r.m.s.d of 0.1 Å for 155 Cα atoms (Fig. 4B). Careful inspection of the structural superimposition of both crystallographic structures did not reveal any structural alterations due to the mutation of C503.

3.4. Redox-dependent modulation within *Ef*AhpF$_{354\text{-}560}$ C503A

While the atomic structure of *Ef*AhpF$_{354\text{-}560}$ C503A did not show a change due to the mutation made, the question was addressed whether redox processes may alter the position of C503 and neighbouring residues in solution. Therefore, WT *Ef*AhpF$_{354\text{-}560}$ was studied in NMR solution studies in the presence and absence of the reducing agent TCEP. As shown in Fig. 5A, uniformly labelled *Ef*AhpF$_{354\text{-}560}$ resulted in

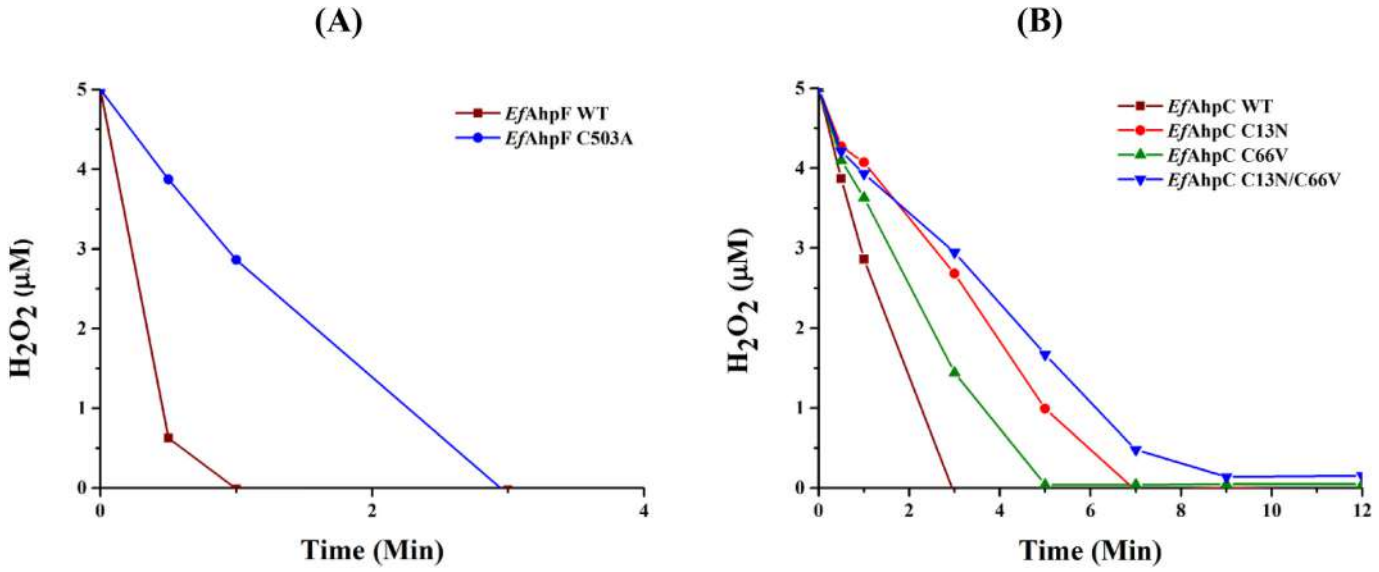

Fig. 3. FOX assay of WT *Ef*AhpF (*brown)* and *Ef*AhpF C503A (*blue*) with *Ef*AhpC (*A*). Data shown are mean of triplicates. (*B*) FOX assay data of *Ef*AhpF C503A with WT *Ef*AhpC (*brown*), *Ef*AhpC C13N (*red*), C66V (*green*) and double-mutant C13N/C66V (*blue*). Data shown are mean of triplicates. (For interpretation of the references to colour in this figure legend, the reader is referred to the Web version of this article.)

a well-dispersed ^{1}H-^{15}N HSQC-spectrum of the protein, indicating proper folding and monodispersity of the recombinant protein. High mobility of the linker region (A314 to Q353), which is included in this construct, gave intense and sharp peaks, which in some cases overlap with other less intense signals. However, this did not affect the overall quality of the spectrum. Sequential backbone assignment based on the triple resonance NMR data, including HNCACB, HNCOCACB, HNCA and HNCOCA enabled the assignment of ^{1}H and ^{15}N resonances for 204 residues out of 234 non-proline residues of *Ef*AhpF$_{354\text{-}560}$. The secondary structure prediction of *Ef*AhpF$_{354–560}$ was performed for the residues W354-A560 based on assigned Cα-chemical shifts, which were subtracted from their random coil values (ΔCα). The prediction is highly consistent with the *Ef*AhpF$_{354\text{-}560}$ crystal structure and reveals eight α-helices and nine β-strands (Fig. 5B).

In comparison, addition of TCEP caused chemical shifts in the ^{1}H-^{15}N HSQC-spectrum of *Ef*AhpF$_{354\text{-}560}$ (Supplementary Fig. S1 and Fig. 5C). Based on the chemical shift perturbation (CSP) analysis between reduced and oxidized *Ef*AhpF$_{314\text{-}560}$, the residues W354, S428, G445, G449, E451-N453, F488, C496, I499-C503, I506, H512, V518, V535, D541, and G548 undergo significant alteration (> 0.1) due to an

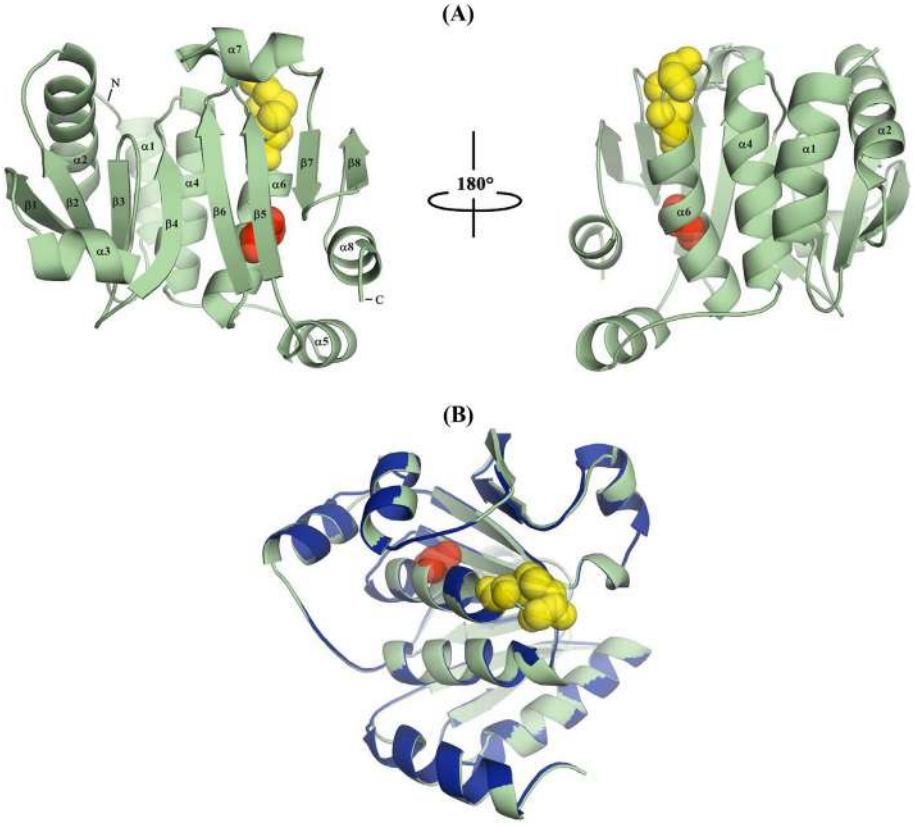

Fig. 4. Cartoon representation of one monomer of the *Ef*AhpF$_{354\text{-}560}$ C503A mutant structure shown in *pale green*, the α-helices and β-strands are labelled (*A*). Catalytic site cysteines 493 and 496 including the disulfide bond are shown in *yellow* spheres. The C503A mutation is shown in *red* spheres. (*B*) *Ef*AhpF$_{354\text{-}560}$ C503A, *pale green* is overlapped with WT *Ef*AhpF$_{354\text{-}560}$, *blue* (PDB ID: 5H29). Catalytic site cysteines 493 and 496, including the disulfide bond, are shown in *yellow* spheres. C503A mutation is shown in *red* spheres. (For interpretation of the references to colour in this figure legend, the reader is referred to the Web version of this article.)

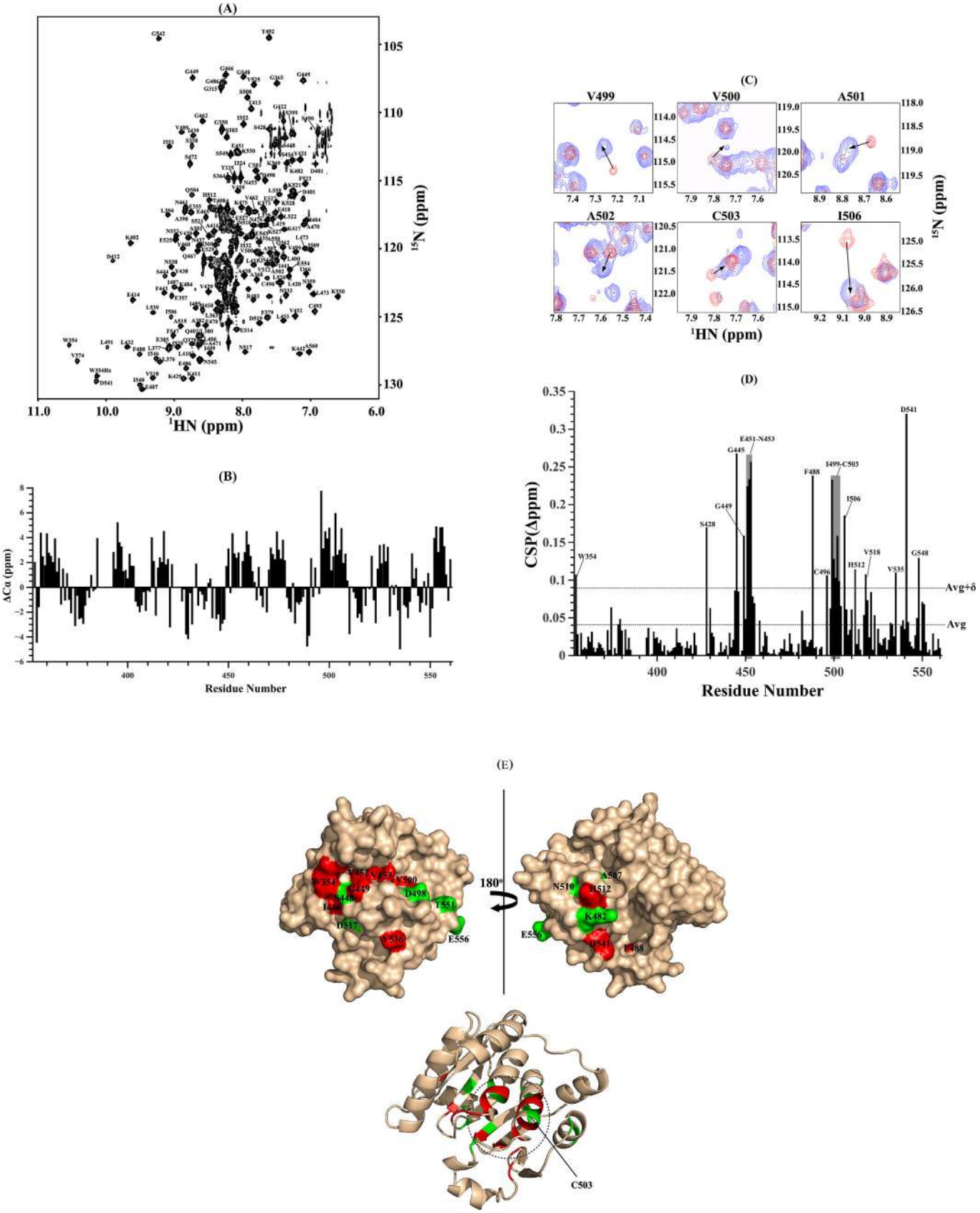

(caption on next page)

Fig. 5. NMR spectroscopic characterization of *Ef*AhpF$_{354-560}$. (*A*)^{15}N-^{1}H TROSY-HSQC-spectrum of *Ef*AhpF$_{354-560}$. The spectrum was recorded at 298K on a Bruker Avance 700 MHz spectrometer. The assignments for resolved backbone residues are labelled with in letter amino acid code and residue number. (*B*) The Cα chemical shift difference (ΔCα) of *Ef*AhpF$_{354-560}$ based on NMR backbone assignment. Contiguous positive and negative chemical shift index values correspond to α-helices and β-strands, respectively. (*C*) Selected sections of some *Ef*AhpF$_{354-560}$ residues showing cross-peaks and undergoing significant changes of chemical shifts during redox modulation. (*D*) Chemical shift perturbation (CSP) analysis between reduced and oxidized *Ef*AhpF$_{354-560}$. Weighted CSPs for the ^{15}N and ^{1}H resonance of reduced and oxidized *Ef*AhpF$_{354-560}$ residues revealing CSP above 0.1 ppm (*solid line*) are labelled as one-letter code. The weighted CSPs between reduced and oxidized *Ef*AhpF$_{354-560}$ for backbone ^{15}N and ^{1}HN were calculated by the formula $\Delta\delta = [(\Delta N/5)^2 + (\Delta HN)^2]^{0.5}$. The average weighted CSP(Avg) and Avg + standard deviation(delta) values were displayed by dashed lines, respectively. (*E*) *(top)* Surface representation of *Ef*AhpF$_{354-560}$ displaying residues showing significant (CSP > 0.1, *red*) and moderate (0.05 < CSP < 0.1, *green*) CSP. (*bottom*) Ribbon representation of CSP analysis. The region which undergoes significant CSP is marked as circle. Amino acid C503, which is located in this region, is shown by stick representation and indicated by a line. (For interpretation of the references to colour in this figure legend, the reader is referred to the Web version of this article.)

alteration of the redox-state (Fig. 5D). As shown in Fig. 5E, the identified residues of *Ef*AhpF$_{354-560}$ involved in redox-dependent modulation form an epitope based on the neighbouring helices α4 and α6 as well as the β-sheets 5 and 6, including C503 of helix α6.

3.5. NMR characterization of a stable *Ef*AhpC-*Ef*AhpF$_{354-560}$ complex formation

Previous studies have shown that AhpF transfers electrons to AhpC through interaction with its thioredoxin-like domain (NTD_N/C) [9,33]. To understand this interaction and decipher the binding epitope, NMR titration experiments were performed, in which uniformly labelled *Ef*AhpF$_{354-560}$ was titrated against *Ef*AhpC. The highly resolved and dispersed NMR-spectrum of *Ef*AhpF$_{354-560}$ mentioned above (Fig. 5A) enabled titration experiments to be performed. The ^{1}H-^{15}N-TROSY-HSQC spectrum was obtained for the labelled *Ef*AhpF$_{354-560}$ protein alone as well as in the presence of increasing amounts of the partner protein *Ef*AhpC (Fig. 6A). During titration experiments, we observed the gradual disappearance or decrease of overall cross peak intensities and line broadening in the ^{1}H-^{15}N-TROSY-HSQC spectra (Fig. 6A–B). Due to the large molecular weight of the *Ef*AhpF$_{354-560}$-*Ef*AhpC complex, the majority of *Ef*AhpF-NTD peaks gradually disappeared, suggesting a global decrease in tumbling, consistent with a stable interaction. Since *Ef*AhpC forms a decamer in solution (about 210 kDa), the above mentioned observation is consistent with a stable complex. However, peaks from amino acid residues in the highly flexible linker region, residues, A314-Q353 showed relatively higher intensities compared with the core part of the protein (W354-A560), indicating that the flexible linker region of the *Ef*AhpF construct was not affected by the interaction with *Ef*AhpC and exhibits a local tumbling motion independent of the global motion of the complex.

3.6. Binding interface of the *Ef*AhpF$_{354-560}$-AhpC complex

To investigate the molecular interaction between *Ef*AhpF$_{354-560}$ and *Ef*AhpC in more detail, NMR-titration data were analyzed in terms of the peak intensities and the line width changes of the NMR spectra between *Ef*AhpF and *Ef*AhpC in the ratio 1:0 and 1:0.1, respectively. The NMR spectra show the significant disappearances or decrease of some cross peak intensities in the ^{1}H-^{15}N TROSY-HSQC spectra compared with other residues (Fig. 6A–B). Plots of intensity ratio (I_O/I_1) before (I_O) and after (I_1) for AhpC (I_O/I_1) and increased line width for indirect ^{15}N dimension at a molar ratio 1:0.1 are shown in Fig. 7A–B. They reveal the candidates of the binding surface of *Ef*AhpF$_{354-560}$ when interacting with *Ef*AhpC. Significant changes in intensity ratio and linewidth over standard deviation were observed for the backbone resonances of residues G449-L455 (Fig. 7A), indicating that these residues are considered as directly involved in the interaction with *Ef*AhpC. Amino acids F355, R360, Q362, F367, I444, I446, G449-L455, Q467, A502, and I506 show intensity changes reflected by the standard deviation values after addition of *Ef*AhpC (Fig. 7A). In addition, the residues including L363, E385, F397, S428, L432, I441, I446, G449-L455, Q467, K475, S490, V500, E525, S534, and M552 reveal increased ^{15}N line-widths over than standard deviation (Fig. 7B).

Based on the NMR intensity changes and linewidth analysis data, the binding area inside *Ef*AhpF, which interacts with *Ef*AhpC, was mapped on the crystal structure of *Ef*AhpF$_{354-560}$ as shown in Fig. 7C, reflecting that surface exposed residues form a well-defined interaction surface around the active site cysteine residue C493. Most surface exposed residues (G449-L455), which show relatively high intensity changes and line width increase form a clustered interaction cleft, indicating that these residues may be strongly related to *Ef*AhpF-AhpC interaction. Residues I441, I446, S448-L455, L490, T492, S521, K527, M531, S532, V533, clustered closely to the catalytically active C493, might also directly participate in *Ef*AhpF-AhpC assembling. In addition, amino acids around the binding epitope such as W354, F355, R360, Q362, S364, Q467 as well as S385, F396, S399, G436, T437, K401, A456, V461, G476, R483, K484, E486, N510, E525, L526, M552 and E554 could be indirectly related to protein-protein interaction as a result of the slight conformational changes of *Ef*AhpF caused by *Ef*AhpC.

3.7. The role of C503 in *Ef*AhpF-AhpC interaction

To shed light into the role of C503 in *Ef*AhpF-AhpC interaction, NMR titration experiments using mutant *Ef*AhpF$_{354-560}$ C503A and *Ef*AhpC (molar ratio 1:0.1) were performed. As displayed in Fig. 8A–C, overall changes of decreasing intensity ratios and increasing line width (^{15}N line width) were observed. Residues G449-N453 of *Ef*AhpF$_{354-560}$ C503A show relatively high intensity ratios compared to other residues, however, the relative intensity changes dramatically decreased (~40%) compared to the WT protein (Fig. 7A–B), indicating overall decreased interaction between *Ef*AhpF$_{354-560}$ C503A and *Ef*AhpC. In addition, the residues showing changes of ^{15}N line width within the *Ef*AhpF$_{354-560}$ C503A mutant after addition of *Ef*AhpC significantly changed (Fig. 8C) when compared to WT (Fig. 7B), indicating that the substitution of C503A affects the interaction between *Ef*AhpF and -AhpC by modulation of protein conformation and dynamic properties. Moreover, ^{1}H-^{15}N-HSQC spectra show disappearance and significant CSPs of the resonances around C503, including residues C496, A501, Q504, A507, S508, N510, H512 and E514 (Fig. 8A). These observations are supporting that the C503A induce changes in conformational and dynamic properties of the residues located around C503, resulting in modulation of the interaction between *Ef*AhpF and -AhpC. In conclusion, it is considered that C503 is not directly involved in protein-protein interaction, but affects the interaction between *Ef*AhpF and -AhpC by the formation of a molecular interaction network with neighbouring residues.

3.8. NMR based docking studies of an *Ef*AhpF-AhpC complex

To investigate the complex formation of *Ef*AhpF-AhpC, the obtained restraints based on the NMR titration experiments and prediction of the interaction residues, were used to drive a HADDOCK-docking simulation [31] as described under Materials and Methods. The top scoring HADDOCK model from the highest scoring cluster was selected (HADDOCK Score −107.8 ± −6.4; Restraint violation energy: 162.4 ± 50.16 Kcal/mol; Buried surface area: 2,403.2 ± 190.8 Å; Z-score: −0.7). The resulting *Ef*AhpF$_{354-560}$-AhpC$_{1-167}$ complex model

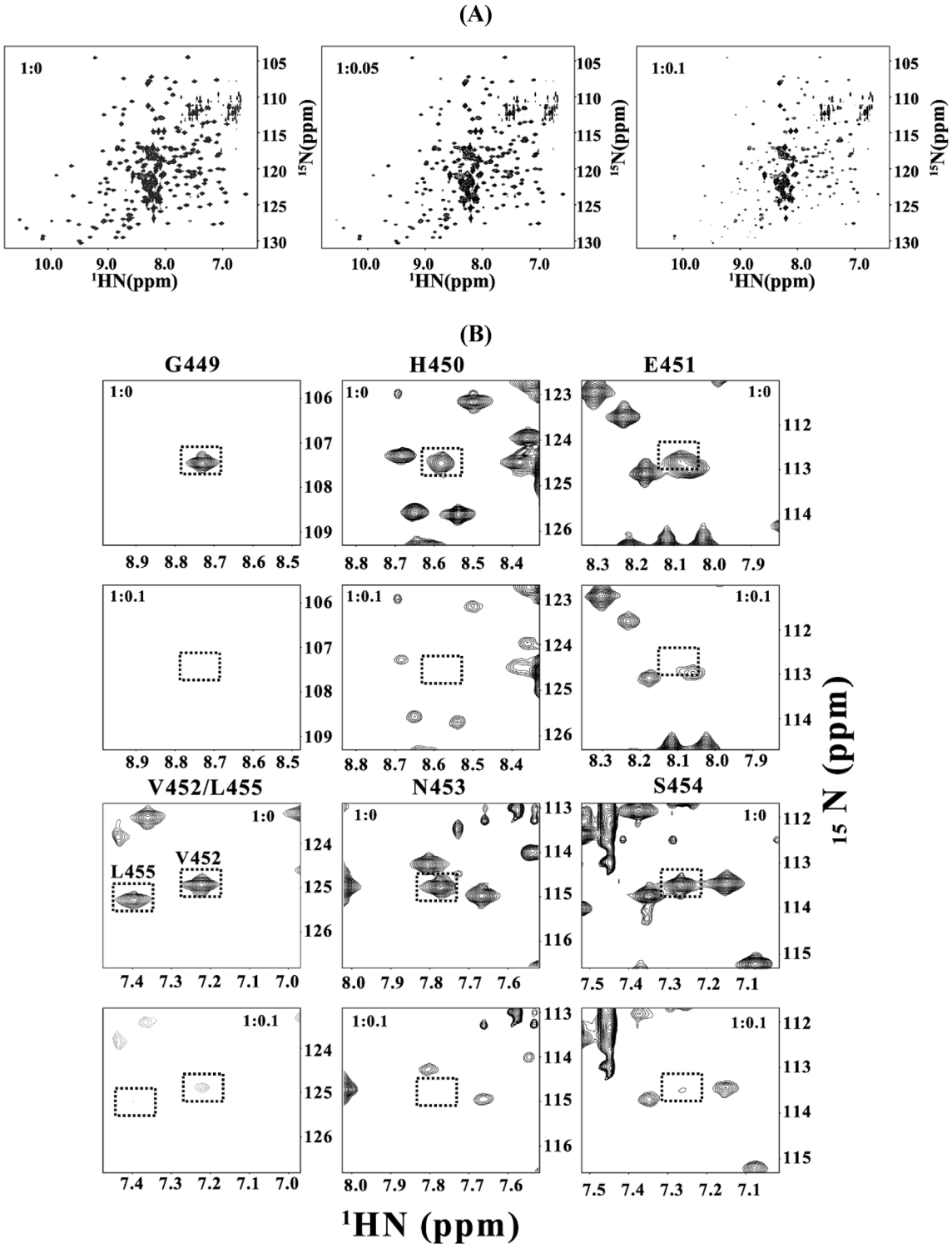

Fig. 6. Interaction of *Ef*AhpC with *Ef*AhpF$_{354\text{-}560}$ as studied by NMR. (*A*) Summary of gradual disappearance and decrease of intensities of the *Ec*AhpF$_{354\text{-}560}$ cross-peaks in the presence of increasing amount of its larger binding partner. A molar ratio of *Ef*AhpF$_{354\text{-}560}$ to *Ef*AhpC of 1:0 (*left*), 1:0.05 (*middle*), and 1:0.1 (*right*) were used. (*B*) Selected sections for some residues show cross-peaks which undergo significant decrease of peak intensities after addition of *Ef*AhpC.

(Fig. 9) indicates the spatial proximity of the regions including the two catalytic cysteine residues C493 and C496 in *Ef*AhpF$_{354\text{-}560}$ with the *Ef*AhpC$_{1\text{-}167}$ dimer. The *Ef*AhpC$_{1\text{-}167}$ dimer contacts this interface mainly with regions including the two helices α2′ of the 1st monomer and α6 of the 2nd monomer (Fig. 9). Helix α6, followed by a loop (residues 161–167) region holding C_R (C166), and α2' helix holding C_P (C47) are linked to form a protein-protein interaction scaffold, which fits into the groove on the binding surface of *Ef*AhpF$_{354\text{-}560}$ (Fig. 9). Residues including G448-L455, S490-F495 comprise the major interaction cleft, forming contact with the binding scaffold of the *Ef*AhpC$_{1\text{-}167}$ dimer.

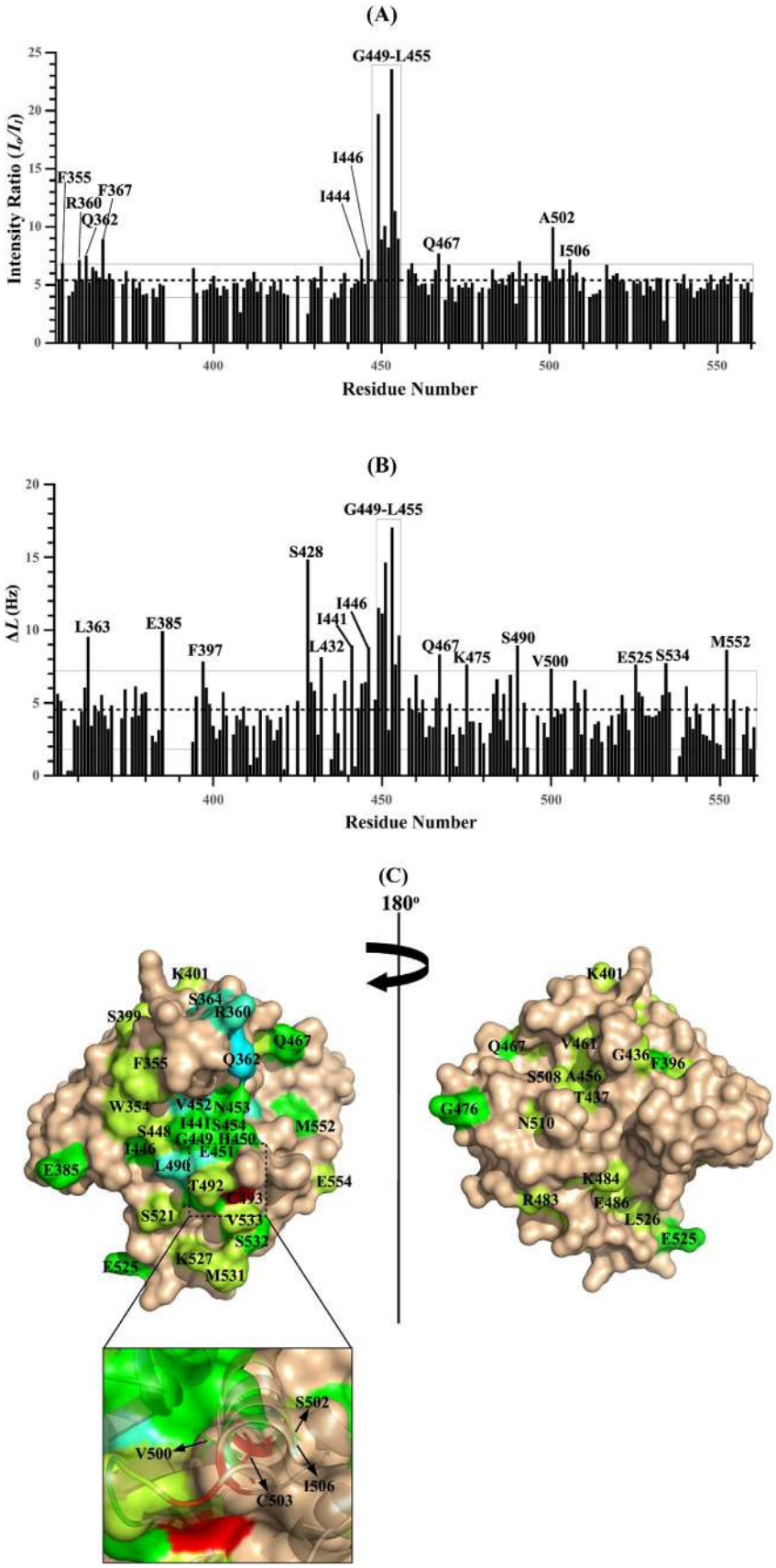

Fig. 7. NMR analysis of *Ef*AhpF$_{354\text{-}560}$ and *Ef*AhpC. The residues of flexible linker regions were excluded from the analysis. (*A*) A plot of changes of peak intensity based on the ratio (I_O/I_1) at a molar ratio of 1:0.1. The average value of the intensity ratio and standard deviation were shown as dotted line and solid box, respectively. The residues showing higher intensity ratio than standard deviation are labelled (*B*) Changes of ^{15}N linewidth between the ^{1}H-^{15}N TROSY-HSQC resonances of *Ef*AhpF$_{354\text{-}560}$ alone and in the presence of *Ef*AhpC at a molar ratio 1:0.1. The average value of the linewidth changes (Δ*L*) and standard deviation were shown as dotted line and solid box, respectively. (*C*) Surface representation of *Ef*AhpF$_{354\text{-}560}$ displaying residues showing significant and moderate decreased intensities (*cyan and green cyan*), and residues showing significant (over than standard deviation) and moderate (over than average) increase of linewidths (*green and light green*). The cysteine catalytic site of *Ef*AhpF$_{314\text{-}560}$ is shown in *red*. (For interpretation of the references to colour in this figure legend, the reader is referred to the Web version of this article.)

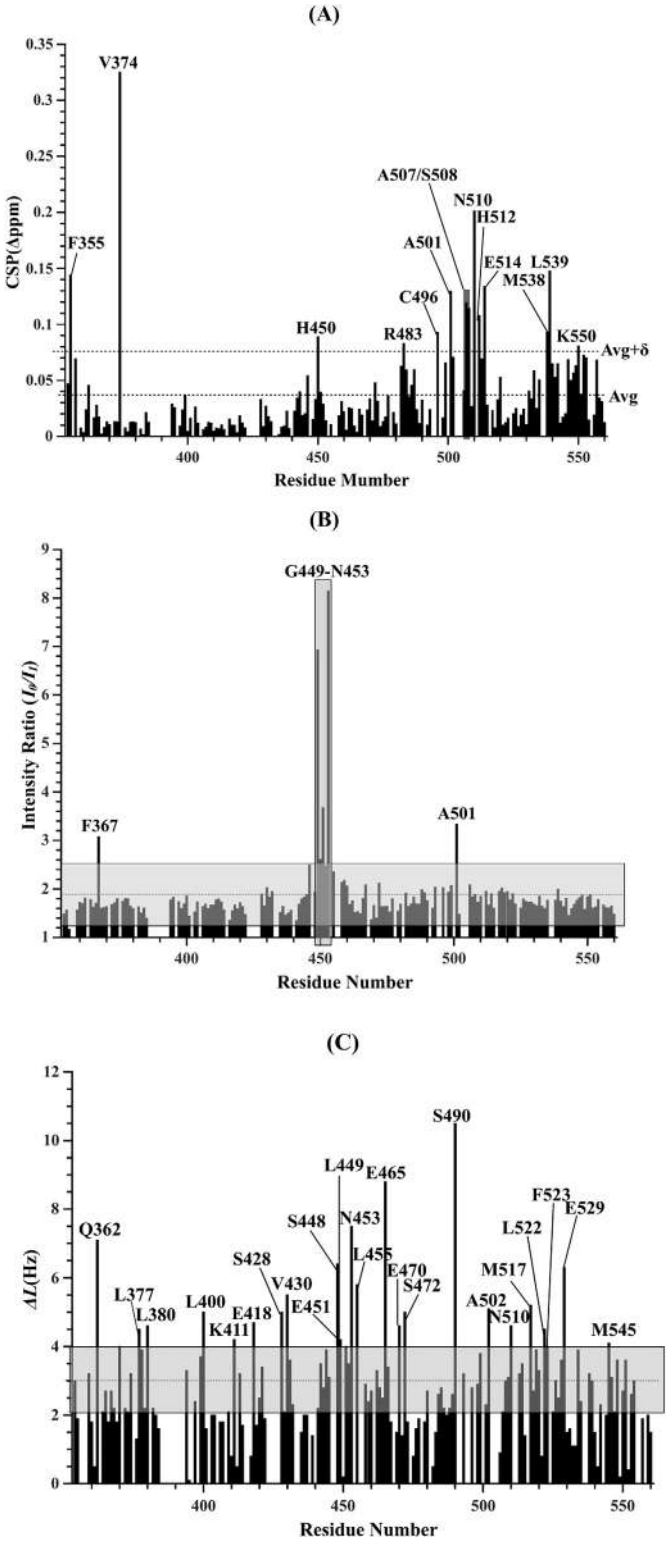

Fig. 8. NMR analysis of mutant *Ef*AhpF$_{354\text{-}560}$ C503A. (*A*) CSP analysis of WT and *mutant Ef*AhpF$_{354\text{-}560}$ C503A. Calculation of weighted CSPs and analysis for the ^{15}N- and ^{1}H resonance of WT and *Ef*AhpF$_{354\text{-}560}$ C503A were performed as described above. The average weighted CSP(Avg) and Avg + standard deviation(delta) values were displayed by dashed lines. Residues over than standard deviations are labelled as one letter code. (*B*) A plot of changes of peak intensity based on the ratio (I_O/I_1) at a molar ratio of 1:0.1. The average value of the intensity ratio and standard deviation were shown as dotted line and solid box, respectively. The residues showing higher intensity ratios than standard deviation are labelled. (*C*) Changes of ^{15}N linewidth between the ^{1}H-^{15}N TROSY-HSQC resonances of *Ef*AhpF$_{354\text{-}560}$ C503A alone and in the presence of *Ef*AhpC at a molar ratio 1:0.1. The average value of the linewidth changes (Δ*L*) and standard deviation were revealed as dotted line and solid box, respectively.

4. Discussion

4.1. Unique features of the E. faecalis (V583) AhpR system

Like the pathogenic *Mycobacterium tuberculosis*, vancomycin-resistant *E. faecalis* (V583) represents a unique AhpR ensemble that evolved a variety of structural variations combined with diverse mechanism to tackle stress caused by ROS. Unlike the well-studied *Ec*AhpC and *St*AhpC, which form a stable decamer in the reduced form and lower weight oligomers in the oxidized state [8–10], the *Mycobacterial* AhpC (*Mtb*AhpC) forms a dodecamer in a reduced state [34,35], while *Ef*AhpC forms a decamer independent to its redox state [7]. The gram-negative *Ec*AhpC and *St*AhpC contain two typical catalytic cysteine residues C_P and C_R [8–10], while *Mtb*AhpC harbours a third cysteine C176, proposed to reduce the disulphide between C_P61 and C_R174 [34]. The gram-positive *Ef*AhpC has two additional cysteines (C13, C66), being relevant for stabilization of the decameric ring and enzyme activity [7].

The electron donor subunit of *Ef*AhpC, *Ef*AhpF, extends these variations for niche adaptation by swapping of the usually N-terminal domain to the C-terminus (NTD_N/C domain) and the CTD:Pyr_redox_2 domain to the N-terminus, a phenomenon discussed by the concept of circular permutation, resulting in improved catalytic activity and altered substrate or ligand binding affinity [36]. Despite the domain swapping, the linker connecting the N- and C-terminal domains in *Ef*AhpF is longer and more diverse in sequence compared to its gram-negative counterparts [13]. Linker mutant studies demonstrated that the length of the linker is required for optimal catalytic activity [13]. In addition, our recent *Ef*AhpF- [13] as well as the presented *Ef*AhpF C503A mutant structure (Fig. 4) revealed the additional $_{409}$ILKDTEPAKELLYGIEKM$_{426}$-loop-helix stretch. Complete and partial deletion of this α3-helix affected protein stability and activity, respectively, identifying Y421 as a critical residue [13]. The unique AhpF α3-helix is proposed to interact with the C-terminus of AhpC, thereby providing efficient electron transfer for AhpC for the final reduction of H_2O_2. Here, we present for the first time that substitution of the extra C503 in *Ef*AhpF increases the K_m for AhpC (70.9 ± 12 μM), resulting in a nearly 27-fold lower catalytic efficiency ($k_{cat}/K_m = 0.7 \times 10^5\,M^{-1}\,s^{-1}$ (Table 2)). These data are in line with a significant reduction in H_2O_2 consumption, indicating the relevance of C503 in electron transfer from the electron donor NADH via the electron centres of *Ef*AhpF to the peroxidatic (C_P47) and resolving (C_R166') cysteine residues in the catalytic centre of *Ef*AhpC, where H_2O_2 is catalysed. Recently, we showed, that substitution of the additional cysteine residues C13 and C66 affect *Ef*AhpC ring stabilization, which was directly related to a reduction of NADH-oxidation and H_2O_2 consumption [7]. The increasing reduction in H_2O_2 decomposition of the mutant ensemble *Ef*AhpC C66V-AhpF C503A followed by *Ef*AhpC C13N-AhpF C503A and *Ef*AhpC C13N/C66-AhpF C503A, respectively (Fig. 3), confirms an additive effect and reflects that these specific *Ef*AhpC-AhpF cysteines are a prerequisite for proper ensemble formation and maximum oxidation of its substrate NADH and the reduction of H_2O_2.

4.2. Important residues of *Ef*AhpF$_{354\text{-}560}$ for the redox process

The NMR solution redox experiment of *Ef*AhpF$_{354\text{-}560}$ sheds light into the residues of the two-fold thioredoxin-like domain (NTD_N/C) which are affected by the process of electron transfer (Fig. 5). The CSP analysis revealed that the residues W354, S428, G445, G449, E451-N453, F488, C496, I499-C503, I506, H512, V518, V535, D641, and

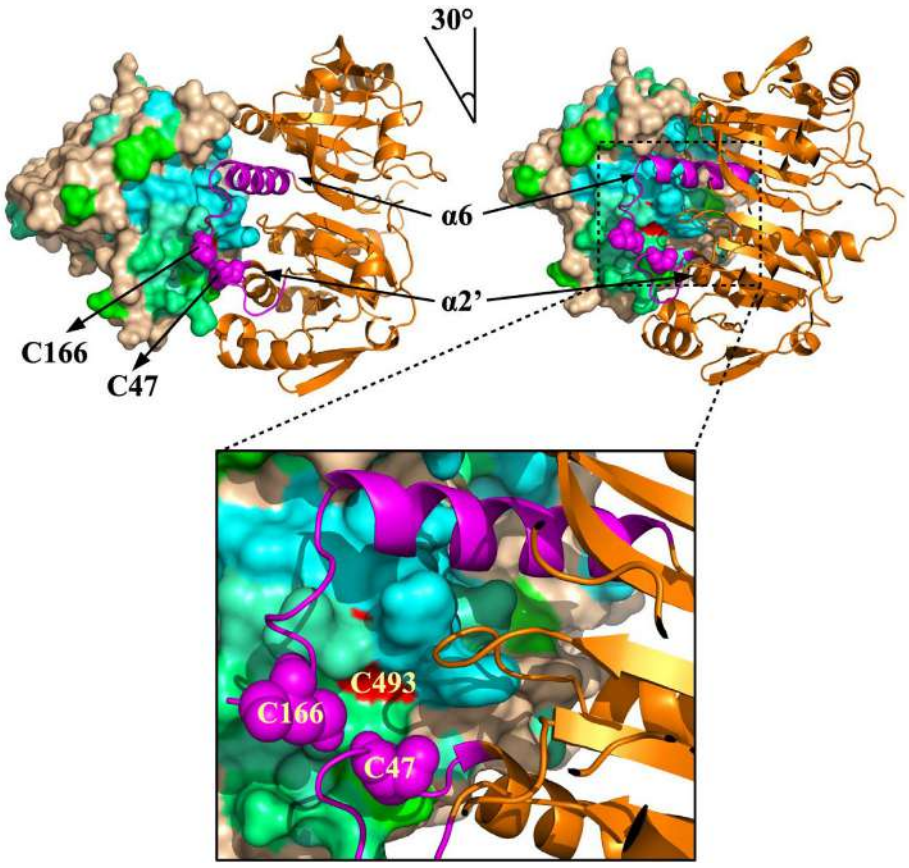

Fig. 9. The best result of HADDOCK docking displaying the *Ef*AhpF$_{354–560}$-AhpC$_{1-167}$ ensemble. (*Upper left panel*) Surface and ribbon representation of the *Ef*AhpF$_{354–560}$-AhpC$_{1–167}$ complex. The major binding contacts of the *Ef*AhpC$_{1-167}$ dimer unit, including helical segment α2' (1st monomer) and α6 (2nd monomer) are labelled and displayed as *magenta*. The catalytic C47 and C166 of *Ef*AhpC$_{1-167}$ are presented as sphere model. (*Upper right panel*) The complex tilted at 30°. (*lower panel*) Extended section of the complex highlighting the catalytic residues C493 (*red*, *Ef*AhpF$_{354-360}$) and C47 (1st monomer of *Ef*AhpC$_{1-167}$). (For interpretation of the references to colour in this figure legend, the reader is referred to the Web version of this article.)

G533 undergo significant alteration due to redox-dependent modulation (Fig. 5C–D). These residues do not only include the extra cysteine C503 but also its close neighbourhood I499 to A502, and I506, which together provide an area formed by the neighbouring helices α4 and α6 as well as the β-sheets 5 and 6 (Fig. 5E). While the comparison of the atomic structures of WT- and mutant *Ef*AhpF$_{354-560}$ C503A nicely demonstrated that the C503 to A mutation does not alter the secondary or tertiary structure of the protein, the NADH oxidation assay and NMR data identify unequivocally its important role for the redox processes within *Ef*AhpF$_{354-560}$.

4.3. Critical binding epitope of *Ef*AhpF$_{354-560}$ for assembling with *Ef*AhpC

The electron transfer pathway after NADH oxidation in the pyridine nucleotide-disulfide oxidoreductase domain (CTD:Pyr_redox_2) of *Ef*AhpF is dictated by conformational changes in the CTD:Pyr_redox_2 as well as by the movement of *Ef*AhpF$_{314-560}$ relative to the CTD:Pyr_redox_2 that enable the redox process between both disulfide centres (C134/C137 and C493/C496) [14,33]. The subsequent rearrangement of *Ef*AhpF$_{354-560}$ to an extended form of *Ef*AhpF brings its disulfide centre C493/C496 in proximity to the redox-active cysteines of *Ef*AhpC. The NMR titration experiment of full length *Ef*AhpC and labelled *Ef*AhpF$_{354-560}$ demonstrate that both *Ef*AhpR subunits interact in a more dynamic and shorter-lived complex (Fig. 6A–B). We recently predicted that the unravelled groove in the atomic structure of *Ef*AhpF$_{354-560}$ wrapping around the protein would provide an area for the packing of the C-terminal tail of *Ef*AhpC [13] as demonstrated for the *E. coli* AhpC [14]. While the C-terminus of *Ef*AhpC would bind to the backside of *Ef*AhpF$_{354-560}$, the disulfide centre C493/C496 of *Ef*AhpF$_{354-560}$ would come in neighbourhood to the catalytic disulphide (C_P47-C_R166) of bound *Ef*AhpC, and thereby providing rapid electron transfer. The titration and docking data presented extend this prediction by identifying the amino acids G448-L455, S490-F495 comprising the major interaction cleft of *Ef*AhpF$_{354-560}$. Interestingly, some of these sequence segments were shown to be involved in the redox process within *Ef*AhpF$_{354-560}$ as well. As highlighted by the inset of Fig. 7C, residues within the proximity of residues V500, S502, the additional C503, and I506, were found to undergo alterations during reduction of the disulfide centre C493/C496 of *Ef*AhpF$_{354-560}$.

To summarize, our study proved the special role of the additional cysteine residue (C503) present in the two-fold thioredoxin-like domain (NTD_N/C) of *Ef*AhpF and that there are alterations in its proximity during redox-state modulation. Moreover, we were able to identify amino acid residues of *Ef*AhpF involved in the interaction with its partner protein *Ef*AhpC and, therefore, to describe the mechanism of electron transfer from *Ef*AhpF to *Ef*AhpC in detail. The data presented here enhance the knowledge of the key enzyme complex AhpR important for ROS defense and ROS homeostasis. The knowledge of systems' special features, the identification of species-specific structures, epitopes and mechanisms, is an excellent basis for future drug development.

Conflicts of interest

The authors declare that they have no conflicts of interest with the contents of this article.

Author contributions

YKT performed most of the experiments, analyzed the data and drafted the manuscript. JS collected and analyzed the NMR data and drafted the manuscript. AMB collected and analyzed the crystallography data and drafted the manuscript. NK collected and analyzed stopped flow data and drafted the manuscript. AG purified labelled and unlabelled proteins and helped editing of the manuscript. FE and BE helped perform the computational analysis and editing of the

manuscript. GG conceived the study and analyzed the data and wrote the manuscript. All authors read and approved the manuscript.

Acknowledgment

This research was supported by a Singapore Ministry of Education Academic Research Fund Tier 1 (RG140/16) to G.G. (M4080811.080). We thank Dr. S. S. M. Malathy for the art work of Fig. 1A.

Appendix A. Supplementary data

Supplementary data to this article can be found online at https://doi.org/10.1016/j.freeradbiomed.2019.04.036.

Abbreviations

H_2O_2	hydrogen peroxide
AhpR	alkyl hydroperoxide reductase
AhpF	alkyl hydroperoxide reductase subunit F
AhpC	alkyl hydroperoxide reductase subunit C
C_P	peroxidatic cysteine
C_R	resolving cysteine
NADH	nicotinamide adenine dinucleotide
CTD:Pyr_redox_2	pyridine nucleotide-disulfide oxidoreductase domain
NTD_N/C	thioredoxin-like domain
FAD	flavin adenine dinucleotide
*Ef*AhpF	*E. faecalis* AhpF
TCEP	tris(2-carboxyethyl)phosphine

References

[1] C.A. Arias, B.E. Murray, The rise of the Enterococcus: beyond vancomycin resistance, Nat. Rev. Microbiol. 10 (2012) 266–278.
[2] M.A. Kohanski, D.J. Dwyer, B. Hayete, C.A. Lawrence, J.J. Collins, A common mechanism of cellular death induced by bactericidal antibiotics, Cell 130 (2007) 797–810.
[3] M. Goswami, S.H. Mangoli, N. Jawali, Involvement of reactive oxygen species in the action of ciprofloxacin against *Escherichia coli*, Antimicrob. Agents Chemother. 50 (2006) 949–954.
[4] J. Lu, A. Holmgren, The thioredoxin antioxidant system, Free Radic. Biol. Med. 66 (2014) 75–87.
[5] X. Wang, X. Zhao, Contribution of oxidative damage to antimicrobial lethality, Antimicrob. Agents Chemother. 53 (2009) 1395–1402.
[6] Y. Arimura, T. Yano, M. Hirano, Y. Sakamoto, N. Egashira, R. Oishi, Mitochondrial superoxide production contributes to vancomycin-induced renal tubular cell apoptosis, Free Radic. Biol. Med. 52 (2012) 1865–1873.
[7] A. Pan, A.M. Balakrishna, W. Nartey, A. Kohlmeier, P.V. Dip, S. Bhushan, G. Grüber, Atomic Structure and enzymatic insights into the vancomycin-resistant *Enterococcus faecalis* (V583) alkylhydroperoxide reductase subunit C, Free Radic. Biol. Med. 115 (2018) 252–265.
[8] P.V. Dip, N. Kamariah, W. Nartey, C. Beushausen, V.A. Kostyuchenko, T.S. Ng, S.M. Lok, W.G. Saw, F. Eisenhaber, B. Eisenhaber, G. Grüber, Key roles of the *Escherichia coli* AhpC C-terminus in assembly and catalysis of alkylhydroperoxide reductase, an enzyme essential for the alleviation of oxidative stress, Biochim. Biophys. Acta Bioenerg. 1837 (2014) 1932–1943.
[9] P.V. Dip, N. Kamariah, M.S. Subramanian Manimekalai, W. Nartey, A.M. Balakrishna, F. Eisenhaber, B. Eisenhaber, G. Grüber, Structure, mechanism and ensemble formation of the alkylhydroperoxide reductase subunits AhpC and AhpF from *Escherichia coli*, Acta Crystallogr. D 70 (2014) 2848–2862.
[10] Z.A. Wood, L.B. Poole, R.R. Hantgan, P.A. Karplus, Dimers to doughnuts: redox sensitive oligomerization of 2-cysteine peroxiredoxins, Biochemistry 41 (2002) 5493–5504.
[11] A. Perkins, K.J. Nelson, D. Parsonage, L.B. Poole, P.A. Karplus, Peroxiredoxins: guardians against oxidative stress and modulators of peroxide signalling, TIBS (Trends Biochem. Sci.) 40 (2015) 435–445.
[12] N. Kamariah, M.S. Manimekalai, W. Nartey, F. Eisenhaber, B. Eisenhaber, G. Grüber, Crystallographic and solution studies of NAD(+)- and NADH-bound alkylhydroperoxide reductase subunit F (AhpF) from *Escherichia coli* provide insight into sequential enzymatic steps, Biochim. Biophys. Acta Bioenerg. 1847 (2015) 1139–1152.
[13] Y.K. Toh, A.M. Balakrishna, M.S.S. Manimekalai, B.B. Chionh, R.R.C. Seetharaman, F. Eisenhaber, B. Eisenhaber, G. Grüber, Novel insights into the vancomycin-resistant *Enterococcus faecalis* (V583) alkylhydroperoxide reductase subunit F, Biochim. Biophys. Acta Gen. Subj. 1861 (2017) 3201–3214.
[14] W. Nartey, S. Basak, N. Kamariah, M.S. Manimekalai, S. Robson, G. Wagner, B. Eisenhaber, F. Eisenhaber, G. Grüber, NMR studies reveal a novel grab and release mechanism for efficient catalysis of the bacterial 2-Cys peroxiredoxin machinery, FEBS J. 282 (2015) 4620–4638.
[15] G. Grüber, J. Godovac-Zimmermann, T.A. Link, Ü. Coskun, V.F. Rizzo, C. Betz, S.M. Bailer, Expression, purification, and characterization of subunit E, an essential subunit of the vacuolar ATPase, Biochem. Biophys. Res. Commun. 298 (2002) 383–391.
[16] Z. Otwinowski, W. Minor, Processing of X-ray diffraction data collected in oscillation mode, Methods Enzymol. 276 (1997) 307–326.
[17] A.J. McCoy, R.W. Grosse-Kunstleve, P.D. Adams, M.D. Winn, L.C. Storoni, R.J. Read, Phaser crystallographic software, J. Appl. Crystallogr. 40 (2007) 658–674.
[18] P. Emsley, K. Cowtan, Coot: model-building tools for molecular graphics, Acta Crystallogr. D 60 (2004) 2126–2132.
[19] G.N. Murshudov, A.A. Vagin, E.J. Dodson, Refinement of macromolecular structures by the maximum-likelihood method, Acta Crystallogr. D 53 (1997) 240–255.
[20] V.B. Chen, W.B. Arendall 3rd, J.J. Headd, D.A. Keedy, R.M. Immormino, G.J. Kapral, L.W. Murray, J.S. Richardson, D.C. Richardson, MolProbity: all-atom structure validation for macromolecular crystallography, Acta Crystallogr. D 66 (2010) 12–21.
[21] P.D. Adams, P.V. Afonine, G. Bunkoczi, V.B. Chen, I.W. Davis, N. Echols, J.J. Headd, L.W. Hung, G.J. Kapral, R.W. Grosse-Kunstleve, A.J. McCoy, N.W. Moriarty, R. Oeffner, R.J. Read, D.C. Richardson, J.S. Richardson, T.C. Terwilliger, P.H. Zwart, PHENIX: a comprehensive Python-based system for macromolecular structure solution, Acta Crystallogr. D 66 (2010) 213–221.
[22] W. DeLano, The *PyMOL* Molecular Graphics System, DeLano Scientific, San Carlos, CA, 2002.
[23] R. Maiti, G.H. Van Domselaar, H. Zhang, D.S. Wishart, SuperPose: a simple server for sophisticated structural superposition, Nucleic Acids Res. 32 (2004) W590–W594.
[24] M.D. Winn, An overview of the CCP4 project in protein crystallography: an example of a collaborative project, J. Synchrotron Radiat. 10 (2003) 23–25.
[25] M.D. Winn, C.C. Ballard, K.D. Cowtan, E.J. Dodson, P. Emsley, P.R. Evans, R.M. Keegan, E.B. Krissinel, A.G. Leslie, A. McCoy, S.J. McNicholas, G.N. Murshudov, N.S. Pannu, E.A. Potterton, H.R. Powell, R.J. Read, A. Vagin, K.S. Wilson, Overview of the CCP4 suite and current developments, Acta Crystallogr. D 67 (2011) 235–242.
[26] D. Rovnyak, D.P. Frueh, M. Sastry, Z.Y. Sun, A.S. Stern, J.C. Hoch, G. Wagner, Accelerated acquisition of high resolution triple-resonance spectra using non-uniform sampling and maximum entropy reconstruction, J. Magn. Reson. 170 (2004) 15–21.
[27] V.Y. Orekhov, V.A. Jaravine, Analysis of non-uniformly sampled spectra with multi-dimensional decomposition, Prog. Nucl. Magn. Reson. Spectrosc. 59 (2011) 271–292.
[28] K. Kazimierczuk, V.Y. Orekhov, Accelerated NMR spectroscopy by using compressed sensing, Angew. Chem. Int. Ed. 50 (2010) 5556–5559.
[29] F. Delaglio, S. Grzesiek, G.W. Vuister, G. Zhu, J. Pfeifer, A. Bax, NMRPipe: a multidimensional spectral processing system based on the UNIX pipes, J. Biomol. NMR 6 (1995) 277–293.
[30] T.D. Goddard, D.G. Kneller, SPARKY, Version 3, University of California, San Francisco, CA, 2007.
[31] S.J. de Vries, M. van Dijk, A.M. Bonvin, The HADDOCK web server for data-driven biomolecular docking, Nat. Protoc. 5 (2010) (2010) 883–897.
[32] S.B. Qin, H.X. Zhou, meta-PPISP: a meta web server for protein-protein interaction site prediction, Bioinformatics 23 (2007) 3386–3387.
[33] L.B. Poole, A. Godzik, A. Nayeem, J.D. Schmitt, AhpF can be dissected into two functional units: tandem repeats of two thioredoxin-like folds in the N-terminus mediate electron transfer from the thioredoxin reductase-like C-terminus to AhpC, Biochemistry 39 (2000) 6602–6615.
[34] B.G. Guimaraes, H. Souchon, N. Honore, B. Saint-Joanis, R. Brosch, W. Shepard, S.T. Cole, P.M. Alzari, Structure and mechanism of the alkyl hydroperoxidase AhpC, a key element of the *Mycobacterium tuberculosis* defense system against oxidative stress, J. Biol. Chem. 280 (2005) 25735–25742.
[35] C.F. Wong, J. Shin, M.S. Subramanian Manimekalai, W.G. Saw, Z. Yin, S. Bhushan, A. Kumar, P. Ragunathan, G. Grüber, AhpC of the mycobacterial antioxidant defense system and its interaction with its reducing partner Thioredoxin-C, Sci. Rep. 7 (2017) 5159.
[36] Y. Yu, S. Lutz, Circular permutation: a different way to engineer enzyme structure and function, Trends Biotechnol. 29 (2011) 18–25.
[37] C. Notredame, D.G. Higgins, J. Heringa, T-coffee: a novel method for fast and accurate multiple sequence alignment, J. Mol. Biol. 302 (2000) 205–217.
[38] A.M. Waterhouse, J.B. Procterm, D.M.A. Martin, M. Clamp, G.J. Barton, Jalview Version 2 – a multiple sequence alignment editor and analysis workbench, Bioinformatics 25 (2009) 1189–1191.